




# Shear performance of microscale ball grid array structure Sn–3.0Ag–0.5Cu solder joints with different surface finish combinations under electro-thermo-mechanical coupled loads

Bo Wang<sup>1,2</sup>, Wangyun Li<sup>1,2,\*</sup> , and Kailin Pan<sup>1,2,\*</sup>

<sup>1</sup>Engineering Research Center of Electronic Information Materials and Devices, Ministry of Education, Guilin University of Electronic Technology, Guilin 541004, China

<sup>2</sup>Guangxi Key Laboratory of Manufacturing System and Advanced Manufacturing Technology, School of Mechanical and Electrical Engineering, Guilin University of Electronic Technology, Guilin 541004, China

**Received:** 21 November 2021

**Accepted:** 29 December 2021

**Published online:**

2 February 2022

© The Author(s), under exclusive licence to Springer Science+Business Media, LLC, part of Springer Nature 2022

## ABSTRACT

The shear performance and fracture behavior of microscale ball grid array structure Sn–3.0Ag–0.5Cu solder joints with different substrate surface finishes (Cu with organic solderability preservatives and electroless Ni/immersion Au) combinations under electro-thermo-mechanical (ETM) coupled loads with increasing current density (from  $1.0 \times 10^3$  to  $6.0 \times 10^3$  A/cm<sup>2</sup>) were systematically investigated by experimental characterization, theoretical analysis, and finite element simulation. The results reveal that the shear strength varies slightly with different surface finish combinations, initially increasing and then decreasing as the current density is increased. Moreover, the increase in current density shifts the fracture location from the solder matrix to the interface between solder and intermetallic compound (IMC) layer, resulting in a ductile-to-brittle transition. The interfacial fracture is triggered by electric current crowding at the groove of the IMC layer and driven by the mismatch strain at the solder/IMC layer interface.

## 1 Introduction

Solder joints function as electrical interconnects, thermal dissipation channels, and mechanical supports in electronics; however, solder joints are considered the weakest links. As electronic devices continue to be miniaturized, the current density flowing through

solder joints significantly increases, resulting in severe Joule heating. As the temperature of the solder joint increases because of the intensified Joule heating [1], strain mismatch occurs due to the different coefficient of thermal expansions (CTE) of materials in the solder joint [2]. Thus, during electronic device operation, solder joints are simultaneously subjected to electrical,

Address correspondence to E-mail: li.wangyun@guet.edu.cn; pankl@guet.edu.cn

thermal, and mechanical loads, known as electro-thermo-mechanical (ETM) coupled loads.

Previous studies have shown that the mechanical performance of solder joints is significantly influenced by ETM coupled loads. As the homologous temperature of most Pb-free solders is over 0.5 at room temperature, creep is a prominent occurrence in solder joints. In addition, both creep and electromigration (EM) are long-term reliability issues in solder joints. Under electric current stressing, the steady-state creep rate increases significantly compared to that of the solder joints without current stressing [3, 4]. However, it has also been reported that the creep rate of solder joints can be lowered by electromigration [5, 6]. In other words, the influence of ETM coupled loads on the creep behavior of solder joints is still ambiguous [3–6]. Besides, for the other long-term deformations of solder joints, such as fatigue and thermal cycling, current stressing sharply decreases their service life and their fracture behavior varies with the current density [7–9]. In contrast, short-term deformations, such as tensile [10–12] and shear behavior [13–17], which are commonly observed in solder joints have received less attention. While, clarifying the influence mechanism of electric current stressing on the tensile and shear performance of solder joints is beneficial in determining the mechanism of electric current stressing on the long-term deformation of solder joints. Recent studies have shown that the tensile and shear strengths of solder joints decrease with increasing current density and their fracture position changes from the solder matrix to the interface between the solder matrix and intermetallic compound (IMC) layer (solder/IMC layer interface) [12–14]. Compared to tensile loading, shear loading is more common in solder joints. Previous studies on the shear performance of solder joints mainly focus on tests under ETM coupled loads at high current densities (more than  $6.0 \times 10^3$  A/cm<sup>2</sup>) [13–15]. However, the current density flowing through flip chip or ball grid array (BGA) solder joints in electronics may be much lower [18]. The shear performance can be also influenced by current stressing with a low current density and a slight increase in the shear strength was captured in a single-interface Sn–1.0Ag–0.5Cu solder joint at  $7.0 \times 10^2$  A/cm<sup>2</sup> [19]. While, the mechanism for this shear strength increase under current stressing remains unclear. Further, the occurrence of this phenomenon in a dual-interface BGA-structured solder joint under

ETM coupled loads with a low current density remains unclear too.

Moreover, substrate surface finishes, such as the widely used Cu with organic solderability preservatives (Cu-OSP, Cu substrate) and electroless nickel/immersion gold (ENIG, Ni substrate), can also affect the shear performance of dual-interface solder joints. Without an applied electric current, the shear strength of the solder joints with Ni substrates is usually higher than those with Cu substrates [20–22]. In addition, solder joints with Ni substrates exhibit a ductile-to-brittle transition, whereas those with Cu substrates have ductile-to-pad lift mode transitions with the increase in shear speed [22]. For the line-type Cu wire/Sn–3.0Ag–0.5Cu (SAC305)/Ni wire solder joints with current stressing, in which the thickness of the surface finishes can be regarded as infinite, interfacial fracture preferentially occurs at the Ni substrate side [23]. However, the actual thickness of the surface finishes in the BGA-structured solder joints is in the submicron to micron range. Thus, dual-interface BGA-structured SAC305 solder joints with different substrate surface finish combinations should have different shear performances and fracture behaviors under electric current stressing.

This study was conducted to explore the influence of substrate surface finish combination on the shear deformation and fracture behavior of BGA-structured SAC305 solder joints under ETM coupled loads with increasing current density from  $1.0 \times 10^3$  to  $6.0 \times 10^3$  A/cm<sup>2</sup>. The variations in the shear strength of the solder joints with different substrate surface finish combinations under current stressing were analyzed in terms of temperature, current density distribution, and strain using experimental characterization, theoretical analysis, and finite element simulation.

## 2 Experimental procedure and simulation method

### 2.1 Experimental procedure

This study fabricated and used BGA-structured solder joints. The diameter of the SAC305 balls was 600 μm. Bismaleimide triazine (BT) epoxy-based substrates, namely, Cu-OSP (Cu substrate) and ENIG (Ni substrate), were used for the fabrication of the solder joints. The thickness of the Cu layer in the Ni

substrate was five times that of the Ni layer. The opening diameter of the pad was 480  $\mu\text{m}$ . The solder joint was fabricated as follows: (1) A SAC305 solder ball was planted on a substrate and reflowed on a BGA rework machine with a typical ramp-soak-spike curve, thereby forming a single-interface joint. (2) A single-interface joint was assembled on another substrate and reflowed. The peak reflow temperature was 250  $^{\circ}\text{C}$  and the dwell time was 50 s. The standoff height of the joint was controlled at 300  $\mu\text{m}$  using Cu wires of the same diameter as the gauge. A mildly activated rosin flux was employed during the reflow. (3) After the reflow, the solder joints were cleaned using an ultrasonic cleaner (DR-MS20) for 10 min. The detailed procedure for preparing the BGA-structured solder joint is shown in Fig. 1. Using this method, Cu/SAC305/Cu, Ni/SAC305/Ni, Ni/SAC305/Cu, and Cu/SAC305/Ni solder joints were prepared. Ni/SAC305/Cu and Cu/SAC305/Ni solder joints were fabricated as representatives for the solder joints with Cu and Ni substrates as the side reflowed twice, respectively.

Shear tests of the solder joints under ETM coupled loads were performed using an experimental system modified basing on a dynamic mechanical analyzer (DMA Q800, TA), see Fig. 2. The temperature of the DMA chamber was maintained at 50  $^{\circ}\text{C}$ . When the set temperature was achieved, the solder joint was imposed with a direct current by a constant current power supply (ANS1560D) and the current density was

$1.0 \times 10^3$ ,  $2.0 \times 10^3$ ,  $3.0 \times 10^3$ ,  $4.0 \times 10^3$ ,  $5.0 \times 10^3$ , or  $6.0 \times 10^3$   $\text{A}/\text{cm}^2$ . After 3 min, a shear force with a constant rate of 1.0  $\text{N}/\text{min}$  was applied to the solder joint. During the operation, the parts of the circuit in contact with the furnace and clamp were insulated. After fracture of the joint, a scanning electron microscope (SEM, Quanta 450, FEI) equipped with an energy-dispersive spectrometer (EDS) was used for the fractography.

## 2.2 Finite element method

The microscale solder joints used in this study make it difficult to accurately obtain the local temperature and strain in the solder joint through experimental methods. Therefore, finite element (FE) simulation using the COMSOL Multiphysics software platform was done to characterize the temperature and strain distribution in the solder matrix. Basing on the EDS results presented in Sect. 3.2, the interfacial IMC between Cu and SAC305 solder was  $\text{Cu}_6\text{Sn}_5$ , whereas that between Ni and SAC305 solder was  $(\text{Cu}, \text{Ni})_3\text{Sn}_4$ . As the physical properties of  $(\text{Cu}, \text{Ni})_3\text{Sn}_4$  vary with the Cu and Ni content,  $\text{Ni}_3\text{Sn}_4$  was used instead of the IMC generated on the Ni side of the joint, in the simulation. The physical parameters of Cu, Ni, SAC305 solder,  $\text{Cu}_6\text{Sn}_5$ , and  $\text{Ni}_3\text{Sn}_4$  are listed in Table 1. To obtain more accurate simulation results, the temperature-dependent values of some parameters were used, as presented in Table 1.

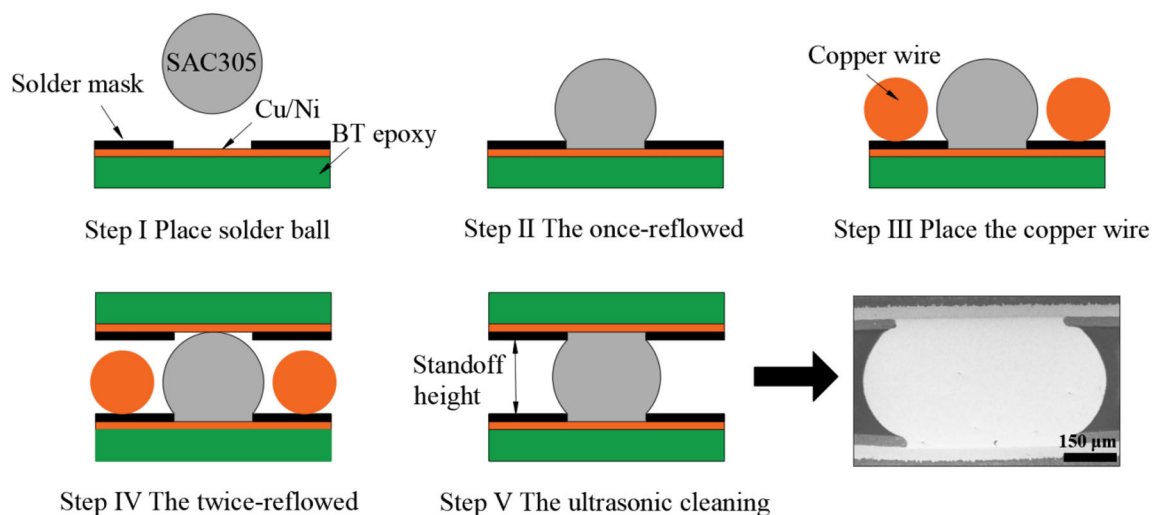
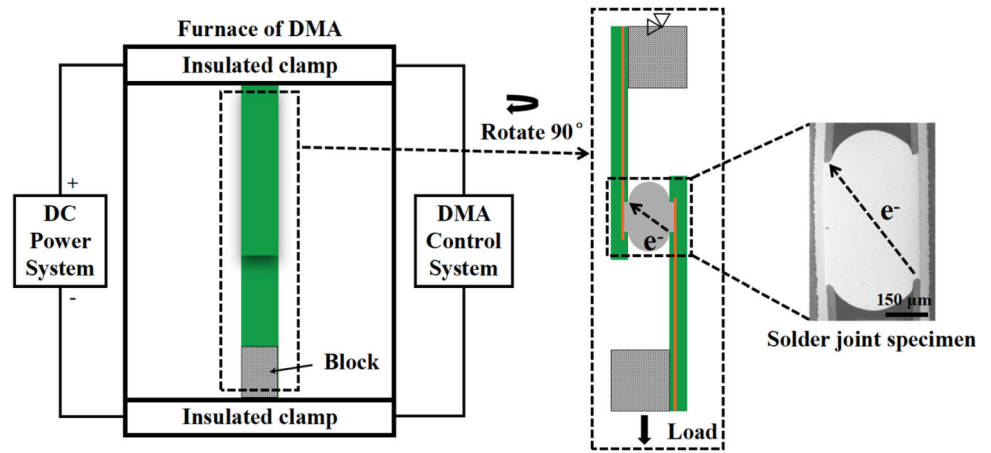


**Fig. 1** Procedure for preparing a BGA-structured solder joint

**Fig. 2** Schematic of the experimental set-up



### 3 Results

#### 3.1 Deformation features

The typical stress–strain curves of the Cu(Ni)/SAC305/Cu(Ni) solder joints under different current densities are shown in Fig. 3. For the Cu/SAC305/Cu solder joint under current densities less than  $5.0 \times 10^3 \text{ A/cm}^2$ , the strain was quite large before the failure of the solder joint, as shown in Fig. 3a, which indicates a prominent ductile fracture. However, when the current density is increased to  $6.0 \times 10^3 \text{ A/cm}^2$ , the strain decreased sharply, suggesting the occurrence of brittle fracture. Accordingly, a ductile-to-brittle transition could occur in the solder joints. Similar deformation behaviors are obtained for the Ni/SAC305/Ni, Ni/SAC305/Cu, and Cu/SAC305/Ni solder joints, as shown in Fig. 3b–d, respectively.

To evaluate the influence of electric current on the deformability of the solder joints, the slope of the

linear deformation stage of the stress–strain curve, which is referred to as the “equivalent elastic modulus,” was calculated, see Fig. 4. Clearly, the equivalent elastic modulus first increases and then decreases with increasing current density and the peak value appears near  $1.0 \times 10^3 \text{ A/cm}^2$ .

To assess the deformability of the solder joints in detail, the average shear strengths are calculated and presented in Fig. 5. For the Cu/SAC305/Cu solder joint with increasing current density, a varying trend of first increasing and then decreasing on the shear strength was captured. At a current density of  $1.0 \times 10^3 \text{ A/cm}^2$ , the shear strength (42.85 MPa) increased compared to that without current stressing (38.40 MPa). The shear strength at  $2.0 \times 10^3 \text{ A/cm}^2$  is almost unchanged comparing to that without current stressing. While, the shear strength continuously decreased at higher current density and it eventually dropped to 5.92 MPa at  $6.0 \times 10^3 \text{ A/cm}^2$ . Clearly, the ETM coupled loads

**Table 1** Materials properties for simulation

Properties	Cu	Ni	SAC305	Cu <sub>6</sub> Sn <sub>5</sub>	Ni <sub>3</sub> Sn <sub>4</sub>
Electrical conductivity (10 <sup>7</sup> S/m)	6.00 [13]	1.28 [24]	0.87 [13]	0.57 [13]	0.35 [24]
Thermal conductivity (W/(m K))	398.0 [24]	90.5 [24]	57.3 [13]	34.1 [13]	19.6 [24]
Density (g/cm <sup>3</sup> )	8.94 [25]	8.90 [24]	7.38 [25]	8.28 [24]	8.65 [24]
Young’s modulus (GPa)	117.0 [24]	213.0 [24]	$E(T)^a$	85.6 [24]	133.3 [24]
Poisson’s ratio	0.35 [13]	0.31 [25]	0.36 [25]	0.31 [13]	0.33 [26]
CTE (10 <sup>-6</sup> /K)	16.6 [24]	12.9 [24]	$CTE_1(T)^b$	$CTE_2(T)^c$	$CTE_3(T)^d$
Specific heat capacity (J/(kg K))	385.2 [24]	439.0 [24]	222.1 [24]	286.0 [24]	272.0 [24]

$$^a E(T) = 70.1449 - 5.20389 \times 10^{-2}T - 3.285 \times 10^{-5}T^2$$

$$^b CTE_1(T) = 7.107264 \times 10^3 - 1.228078 \times 10^{-4}T + 5.714812 \times 10^{-7}T^2$$

$$^c CTE_2(T) = -7.4583 \times 10^{-6} - 2.3575 \times 10^{-7}T + 7.3884 \times 10^{-10}T^2$$

$$^d CTE_3(T) = 1.4192 \times 10^{-5} - 8.75 \times 10^{-9}T + 2.9762 \times 10^{-11}T^2$$

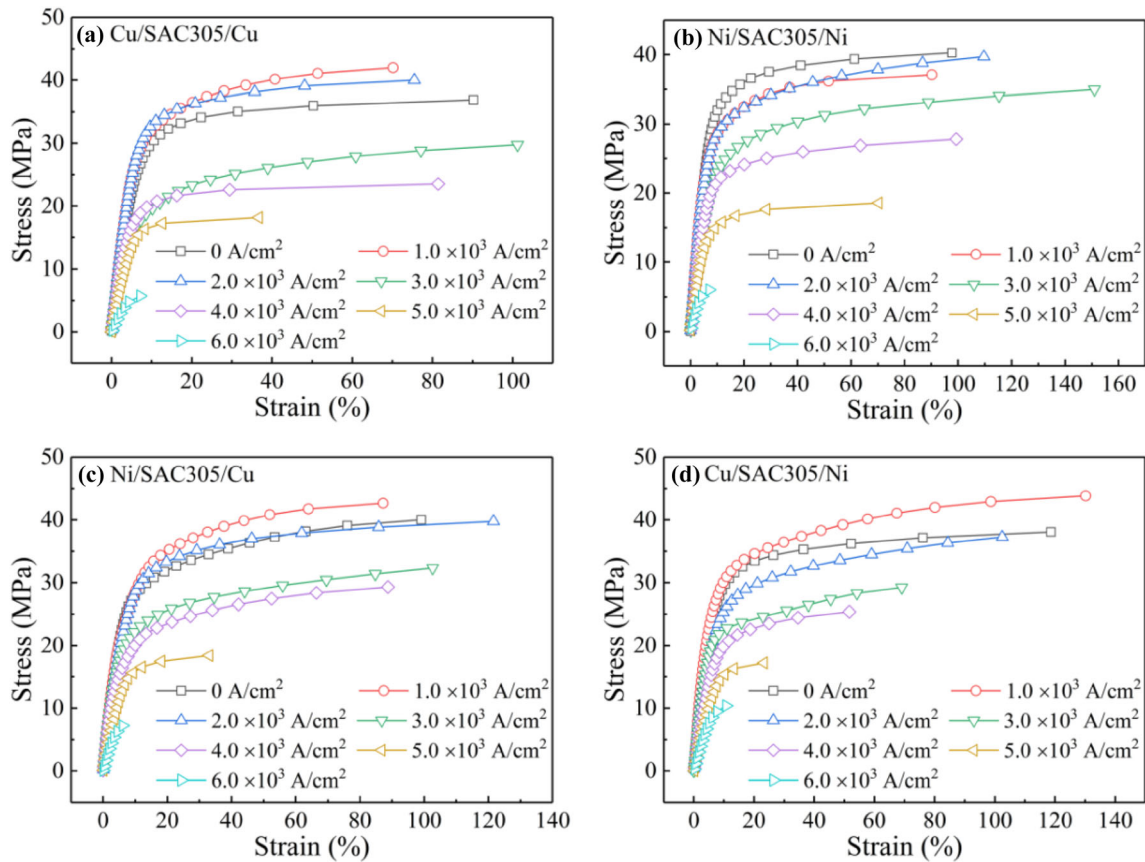


**Fig. 3** Typical stress–strain curves of the BGA-structured solder joints with different current densities, **a** Cu/SAC305/Cu, **b** Ni/SAC305/Ni, **c** Ni/SAC305/Cu, and **d** Cu/SAC305/Ni

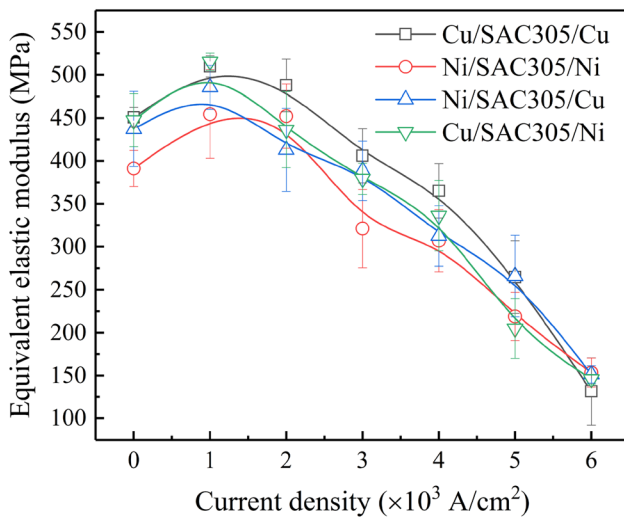


**Fig. 4** Equivalent elastic modulus of the joints with increasing current density

with a relatively high current density led to the severe deterioration of the shear performance of the solder joints.

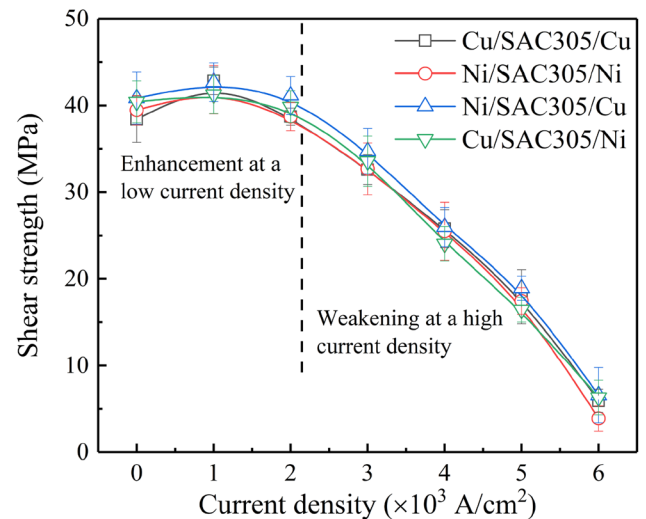


**Fig. 5** Shear strength of the joints with different current densities

In general, there are two stages for the influence of the current stressing on the shear strength, including the enhancement stage at a low current density and weakening stage at a high current density. The

graphs of the shear strengths with increasing current density coincide for all solder joint samples. Moreover, the shear strengths of the Cu(Ni)/SAC305/Cu(Ni) solder joints at the same current density are generally similar.

In order to evaluate the damage induced by the ETM coupled loads to the solder joints, the shear strength change rate of the solder joints at different current densities was calculated by comparing the average shear strength of the solder joint with and without current stressing, as shown in Fig. 6. For the Cu/SAC305/Cu solder joints, the shear strength change rate showed a similar varying trend as that of shear strength. At  $1.0 \times 10^3$  A/cm<sup>2</sup>, the average shear strength increase rate was 11.57%. At  $2.0 \times 10^3$  A/cm<sup>2</sup>, the shear strength increase rate decreased to near zero. Whereafter, the average shear strength sharply decreased at a rate of 15.15 to 93.87% with increasing current density from  $3.0 \times 10^3$  to  $6.0 \times 10^3$  A/cm<sup>2</sup>, as shown in Fig. 6a, indicating the accelerating damage to the solder joints. Similar results are also observed for other solder joints, as shown in Fig. 6b–d.

### 3.2 Fracture behavior

The fracture morphologies of the Cu/SAC305/Cu solder joints under ETM coupled loads are shown in Fig. 7. Without current stressing, dimples are scattered on the fracture surface of the solder joint, see Fig. 7a, showing typical ductile fracture feature [27]. The fracture surface of the solder joints at  $1.0 \times 10^3$  A/cm<sup>2</sup> is similar to that without current stressing, see Fig. 7b. The magnified zone region 1 in Fig. 7b reveals the numerous small dimples in the fracture morphology, which confirms the ductile fracture at a current density of  $1.0 \times 10^3$  A/cm<sup>2</sup>. Similarly, fracture surfaces with obvious dimples are also noted at the current density range of  $2.0 \times 10^3$ – $4.0 \times 10^3$  A/cm<sup>2</sup>, see Fig. 7c–e. Obviously, the fracture remains in the solder matrix at a current density up to  $4.0 \times 10^3$  A/cm<sup>2</sup> and the height from the fracture surface to the Cu-OSP surface finish is approximately equal to the thickness of the solder mask. Moreover, under current densities no less than  $2.0 \times 10^3$  A/cm<sup>2</sup>, the local melting of the solder is noted at the fracture surface and the melting region expanded with increasing current density, see Fig. 7c–f. As the

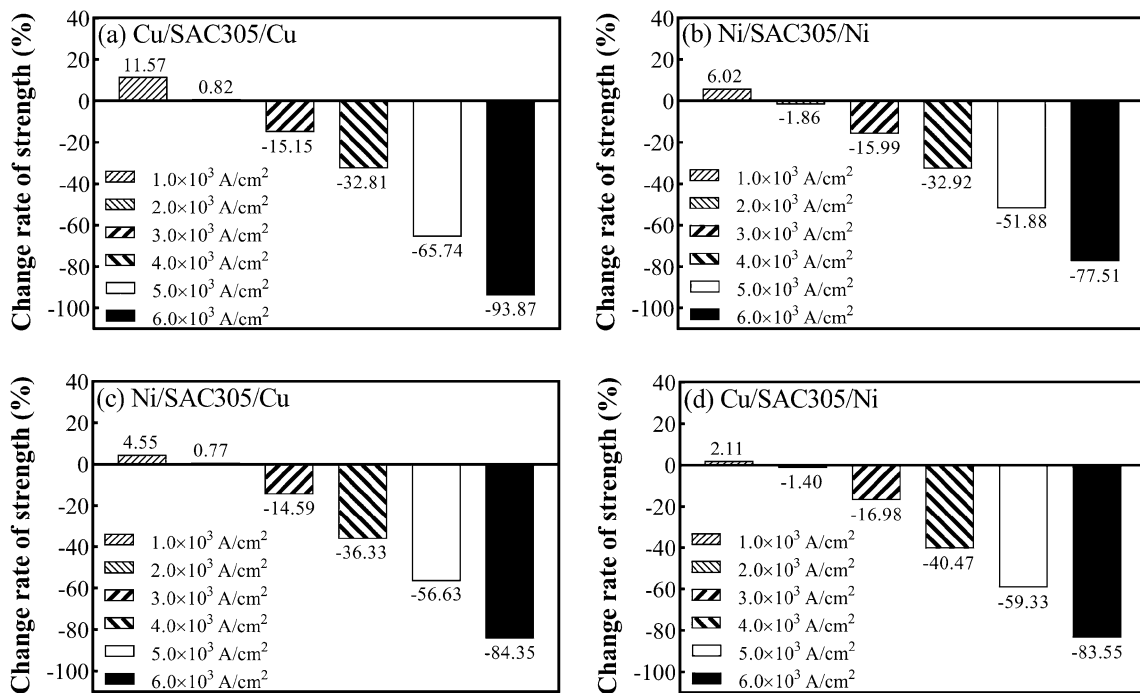


**Fig. 6** Shear strength change rate of the joints under ETM coupled loads, **a** Cu/SAC305/Cu, **b** Ni/SAC305/Ni, **c** Ni/SAC305/Cu, and **d** Cu/SAC305/Ni

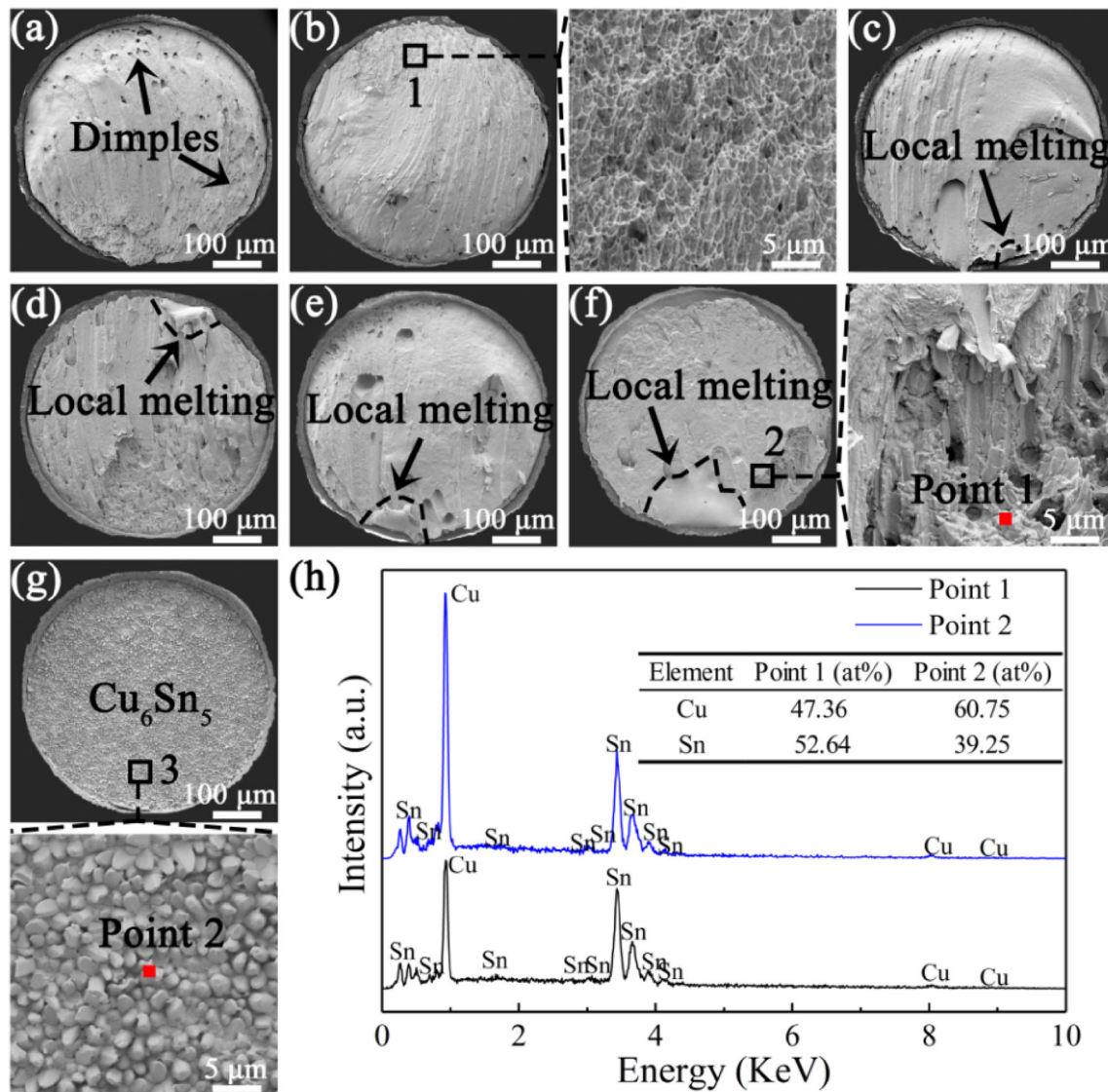


**Fig. 7** Fracture morphology of the BGA-structured Cu/SAC305/Cu solder joints, **a** without current stressing and with a current density of **b**  $1.0 \times 10^3$ , **c**  $2.0 \times 10^3$ , **d**  $3.0 \times 10^3$ , **e**  $4.0 \times 10^3$ , **f**  $5.0 \times 10^3$ , and **g**  $6.0 \times 10^3$  A/cm<sup>2</sup>. **h** EDS results

current density increased to  $5.0 \times 10^3$  A/cm<sup>2</sup>, the dimples almost disappeared and some particles appeared near the local melting region, see Fig. 7f. When the current density reached  $6.0 \times 10^3$  A/cm<sup>2</sup>, the particles occupied almost the entire fracture surface, suggesting typical brittle fracture [28], see Fig. 7g. The EDS results revealed that the atomic ratio of Sn to Cu of the particles in region 2 (point 1) (Fig. 7f) and region 3 (point 2) (Fig. 7g) is approximately 6:5, see Fig. 7h; hence, the particles are Cu<sub>6</sub>Sn<sub>5</sub>. This means the fracture partially occurred at the solder/IMC layer interface at  $5.0 \times 10^3$  A/cm<sup>2</sup> and it

turned to be at the solder/IMC layer interface complete at  $6.0 \times 10^3$  A/cm<sup>2</sup>. Hence, the fracture location gradually shifted from the solder matrix to the solder/IMC layer interface with increasing current density, exhibiting an obvious ductile-to-brittle transition.

The fracture morphologies of the Ni/SAC305/Ni solder joints are shown in Fig. 8. Without current stressing or at  $1.0 \times 10^3$  A/cm<sup>2</sup>, the fracture of the Ni/SAC305/Ni solder joints is similar to that of the Cu/SAC305/Cu solder joints, see Fig. 8a and b. Although the dimples in regions 1 and 2 indicate

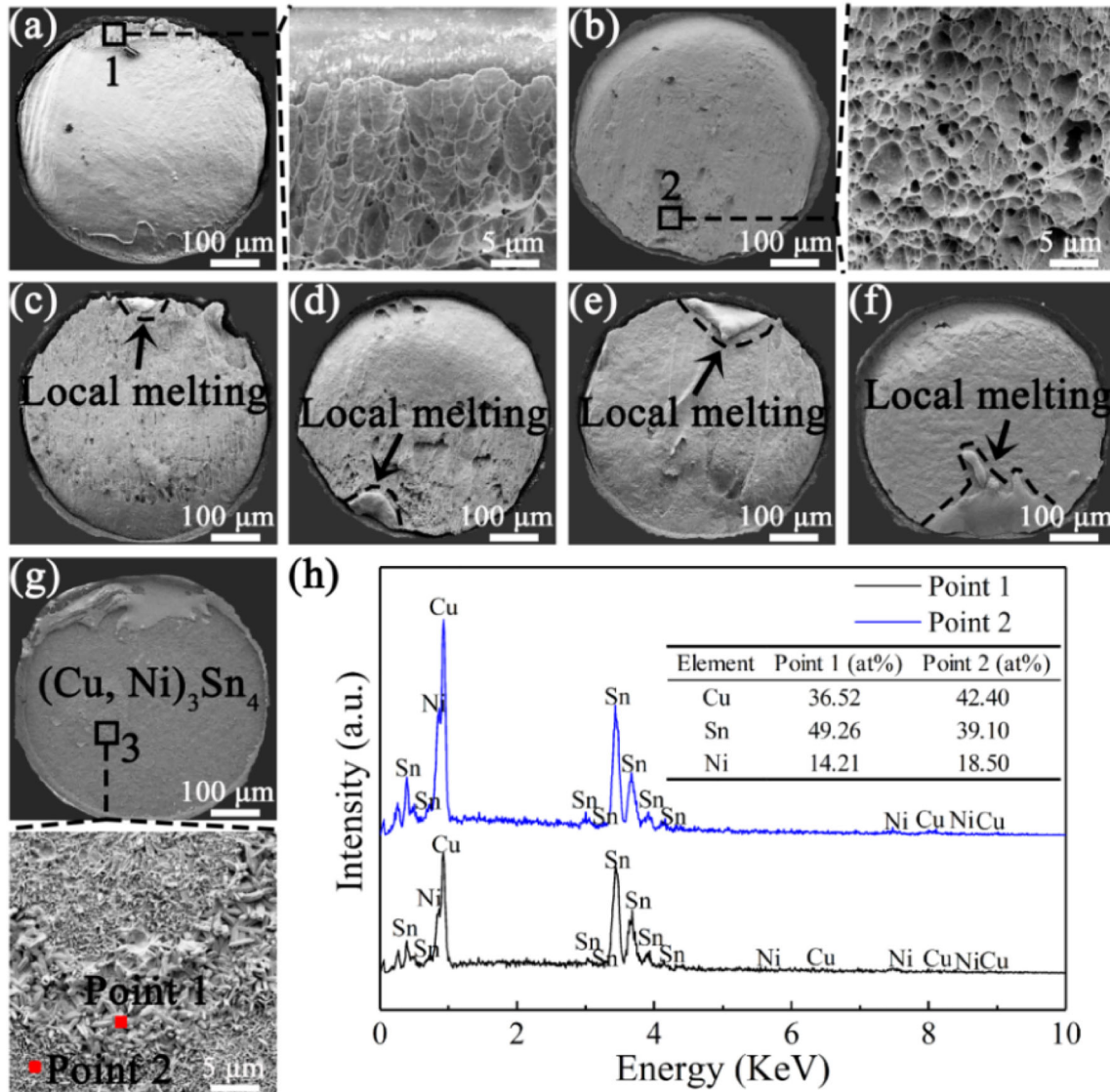


**Fig. 8** Fracture morphology of the BGA-structured Ni/SAC305/Ni solder joints, **a** without current stressing and with a current density of **b**  $1.0 \times 10^3$ , **c**  $2.0 \times 10^3$ , **d**  $3.0 \times 10^3$ , **e**  $4.0 \times 10^3$ , **f**  $5.0 \times 10^3$ , and **g**  $6.0 \times 10^3$  A/cm<sup>2</sup>. **h** EDS results

prominent ductile fracture, the number of dimples gradually decreases with increasing current density and the dimple almost disappeared on the fracture surface at  $5.0 \times 10^3$  A/cm<sup>2</sup>, see Fig. 8c–f. The needle-like  $(\text{Cu, Ni})_3\text{Sn}_4$  particles occupied the majority of the fracture surface at  $6.0 \times 10^3$  A/cm<sup>2</sup>, see Fig. 8g and h. Thus, the fracture location shifted from the solder matrix to the solder/IMC layer interface and a ductile-to-brittle transition occurred as those in the Cu/SAC305/Cu solder joints. Similar fracture characteristics were also observed in the Ni/SAC305/Cu and Cu/SAC305/Ni solder joints with increasing current density, as shown in Figs. 9 and 10.

## 4 Discussion

### 4.1 Shear strength of the solder joints under ETM coupled loads

Usually, the Joule heating-induced temperature ( $T_{\text{Joule}}$ ) in the solder joint is higher than the test temperature. According to Joule’s first law, the Joule heat ( $Q$ ) in the solder matrix can be defined as:

$$Q = I^2Rt = (jA)^2 \left( \rho_R \frac{H}{A} \right) t = j^2 \rho_R A H t, \tag{1}$$

where  $I$  is the applied current,  $R$  is the resistance of the SAC305 solder,  $t$  is the electric current stressing



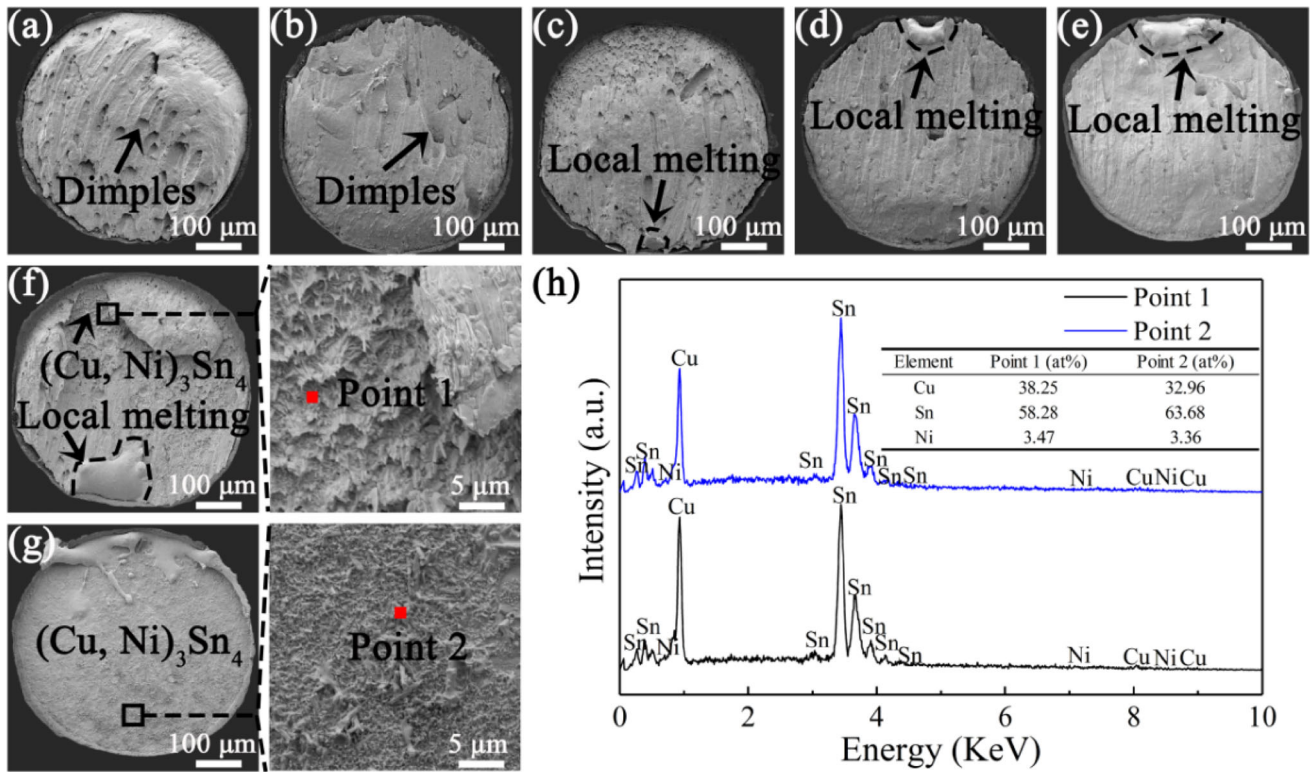


**Fig. 9** Fracture morphology of the BGA-structured Ni/SAC305/Cu solder joints, **a** without current stressing and with a current density of **b**  $1.0 \times 10^3$ , **c**  $2.0 \times 10^3$ , **d**  $3.0 \times 10^3$ , **e**  $4.0 \times 10^3$ , **f**  $5.0 \times 10^3$ , and **g**  $6.0 \times 10^3$  A/cm<sup>2</sup>. **h** EDS results

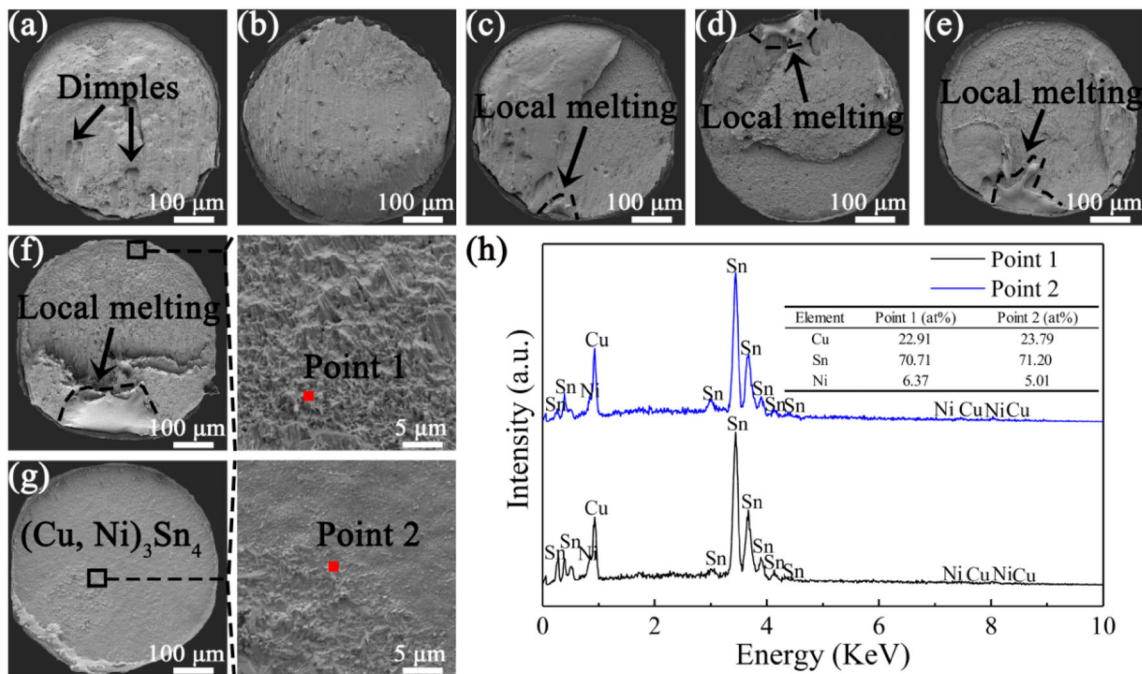


**Fig. 10** Fracture morphology of the BGA-structured Cu/SAC305/Ni solder joints, **a** without current stressing and with a current density of **b**  $1.0 \times 10^3$ , **c**  $2.0 \times 10^3$ , **d**  $3.0 \times 10^3$ , **e**  $4.0 \times 10^3$ , **f**  $5.0 \times 10^3$ , and **g**  $6.0 \times 10^3$  A/cm<sup>2</sup>. **h** EDS results

time,  $j$  is the applied current density,  $A$  is the cross-sectional area of the solder joint,  $\rho_R$  is the resistivity of the SAC305 solder, and  $H$  is the height of the solder joint. Assuming convection as the main heat dissipation method in the solder joint, the heat loss ( $Q_0$ ) can be expressed as [13]:

$$Q_0 = q_0St = h(T_a - T_{\text{Joule}})St, \tag{2}$$

where  $q_0$  is the convective flux,  $S$  is the surface of heating transfer,  $h$  is the heat transfer coefficient, and  $T_a$  is the ambient temperature. From the relationship between temperature and energy,

$$Q + Q_0 = Cm\Delta T = Cm(T_{\text{Joule}} - T_a), \tag{3}$$

where  $C$  is the specific heat of the SAC305 solder and  $m$  is the mass of the solder matrix. By substituting Eqs. (1) and (2) into Eq. (3),  $T_{\text{Joule}}$  can be expressed as:

$$T_{\text{Joule}} = \frac{j^2\rho_R AHt}{hSt + Cm} + T_a. \tag{4}$$

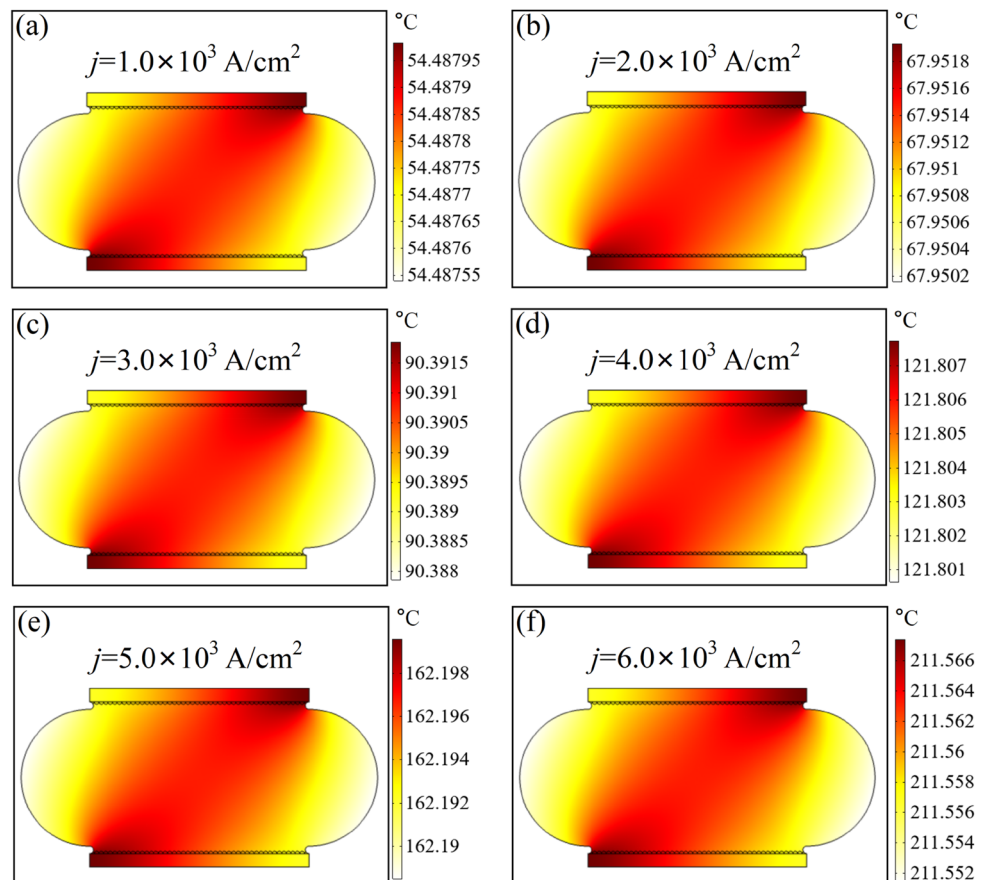
Using Eq. (4), the temperature distribution in the Cu/SAC305/Cu solder joints was obtained from the FE simulation results, see Fig. 11, and  $T_{\text{Joule}}$  increased

with increasing current density. At the same current density, the average temperatures of the Cu(Ni)/SAC305/Cu(Ni) solder joints are approximately equal, as shown in Fig. 12. This can be attributed to the smaller thickness of the Ni layer, which is approximately one-fifth of that of the Cu layer in the Ni substrate. Although more Joule heat is generated in the solder joints with the Ni substrate owing to the higher electric resistivity of Ni (Ni,  $6.84 \mu\Omega\text{-cm}$ ; Cu,  $1.85 \mu\Omega\text{-cm}$ ), heat can be easily dissipated through the Cu layer because of its significantly higher thermal conductivity (Table 1).

Since the Young’s modulus of the solder decreases with increasing temperature [29], the shear strength of the solder joints should decrease monotonically with increasing current density if Joule heat is the dominance. However, this deduction is contradicted by the results shown in Fig. 5. Therefore, another factor is influencing the shear strength under ETM coupled loads.

In addition to Joule heating, athermal effects can also be ascribed to the current stressing in the solder joints [30]. One of the prominent athermal effects is

**Fig. 11** Temperature distribution of the BGA-structured Cu/SAC305/Cu solder joints at **a**  $1.0 \times 10^3$ , **b**  $2.0 \times 10^3$ , **c**  $3.0 \times 10^3$ , **d**  $4.0 \times 10^3$ , **e**  $5.0 \times 10^3$ , and **f**  $6.0 \times 10^3$  A/cm<sup>2</sup>



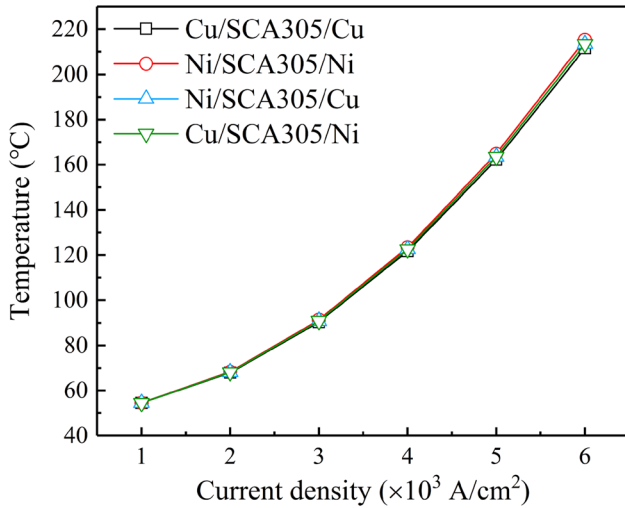


**Fig. 12** Average temperature of the joints with different current densities

the generation of a large number of dislocations in the solder matrix [31–33]. Because of the collision between electrons and metal atoms, a force along the direction of the electron flow, that is, the electron wind force ( $F_W$ ), is imposed on the atoms, which can be expressed as [34]:

$$F_W = Z^* e \rho_R j, \tag{5}$$

where  $Z^*$  is the effective charge (equals to  $-18$  [35], where the negative sign indicates that the Sn atom moves toward the anode side),  $e$  is the electric charge ( $1.602 \times 10^{-19}$  C),  $\rho_R$  is the resistivity ( $1.09 \times 10^{-5}$   $\Omega \cdot \text{cm}$  [36]), and  $j$  is the current density. The electron wind force at  $1.0 \times 10^3$  A/cm $^2$  is calculated to be  $3.14 \times 10^{-18}$  N.

Since the diffusion activation energy of the metal atoms should be overcome during the motion and the activation energy of diffusion of Sn ( $Q_{c\text{-axis}}$ ) in the  $c$ -axis direction is 107.1 kJ/mol, which is higher than that in the  $a/b$ -axis direction, 105 kJ/mol [37]. Therefore, the average activation energy for diffusion per Sn atom ( $Q_{\text{atom}}$ ) can be estimated as:

$$Q_{\text{atom}} = \frac{Q_{c\text{-axis}}}{N_A} = 1.78 \times 10^{-19} \text{ Nm}. \tag{6}$$

Thus, the electron wind force of  $3.14 \times 10^{-18}$  N at  $1.0 \times 10^3$  A/cm $^2$  can drive the atom to move at a distance of 17.6 m, which is significantly larger than the threshold value for generating dislocation in nanoscale.

The large number of dislocations causes lattice stress ( $\sigma$ ) in the solder matrix, which can be described as a function of the dislocation density according to Taylor’s relation [38]:

$$\sigma = \alpha G b d^{1/2}, \tag{7}$$

where  $\alpha$  is the dislocation interaction constant,  $G$  is the shear modulus,  $b$  is the Burgers vector, and  $d$  is the dislocation density. Moreover, the relationship between microhardness ( $H$ ) and stress is as follows [39]:

$$H = 3\sigma = 3\alpha G b d^{1/2}. \tag{8}$$

Clearly, the microhardness increased with the rise of dislocation density. As the strength of metals is positively correlated with their microhardness [40], the shear strength of the solder joints should be elevated with an increase in the dislocation density.

As mentioned above, Joule heating and the athermal effect of current stressing can contribute to the variations in the shear strength of the solder joints under ETM coupled loads. These factors have contrasting influences, as shown in Fig. 13. At  $1.0 \times 10^3$  A/cm $^2$ , the temperature rise in the solder joints does not exceed 5 °C and the Joule heating-induced strength decrease is not prominent, whereas the shear strength is improved owing to the generated dislocations. Thus, a higher shear

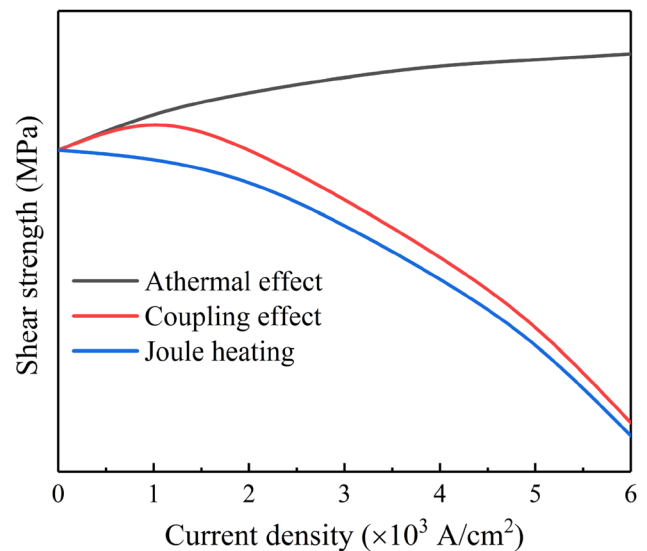


**Fig. 13** Contribution graph of Joule heating and athermal effect to the shear strength of BGA-structured Cu(Ni)/SAC305/Cu(Ni) solder joints under ETM coupled loads

strength is obtained at  $1.0 \times 10^3 \text{ A/cm}^2$  than that without current stressing. This phenomenon is similar to the increase in the shear strength of a single-interface SAC105 solder joint at  $7.0 \times 10^2 \text{ A/cm}^2$  [19]. The slightly higher current density for the shear strength increase in the present study may be attributed to the better heat dissipation in the dual-interface BGA-structured SAC305 solder joint. At  $2.0 \times 10^3 \text{ A/cm}^2$ , the contrasting influences of the current stressing on the shear strength of the solder joints are equal. Hence, the shear strength remained approximately constant compared to that without current stressing. As the current density is further increased,  $T_{\text{Joule}}$  increased sharply (Eq. 4 and Fig. 12); thus, the generated dislocations can be more easily diminished at higher temperatures [41]. In other words, the Joule heating-induced deterioration of the shear strength is more prominent than the athermal effect-induced improvement of the shear strength of the solder joints. Accordingly, the shear strength of the solder joint continued to decrease at a current density of more than  $2.0 \times 10^3 \text{ A/cm}^2$ . In general, the shear strength of the solder

joints first increased and then decreased with increasing current density.

#### 4.2 Fracture mechanism of the solder joints under ETM coupled loads

The solder joints with increasing current density demonstrated a gradual transition of the fracture location from the solder matrix to the solder/IMC layer interface. Three fracture modes of the solder joints under ETM coupled loads are illustrated in Fig. 14. When the current density is  $1.0 \times 10^3$  to  $4.0 \times 10^3 \text{ A/cm}^2$ , the solder joint fractures in the solder matrix and distance from the fracture surface to the surface finish is approximately equal to the height of the solder mask, as shown in Fig. 14a. As the current density increased to  $5.0 \times 10^3 \text{ A/cm}^2$ , the fracture partially occurred in the solder matrix and at the solder/IMC layer interface, as shown in Fig. 14b. At a current density of  $6.0 \times 10^3 \text{ A/cm}^2$ , the interfacial fracture tends to be the dominant fracture, as shown in Fig. 14c.

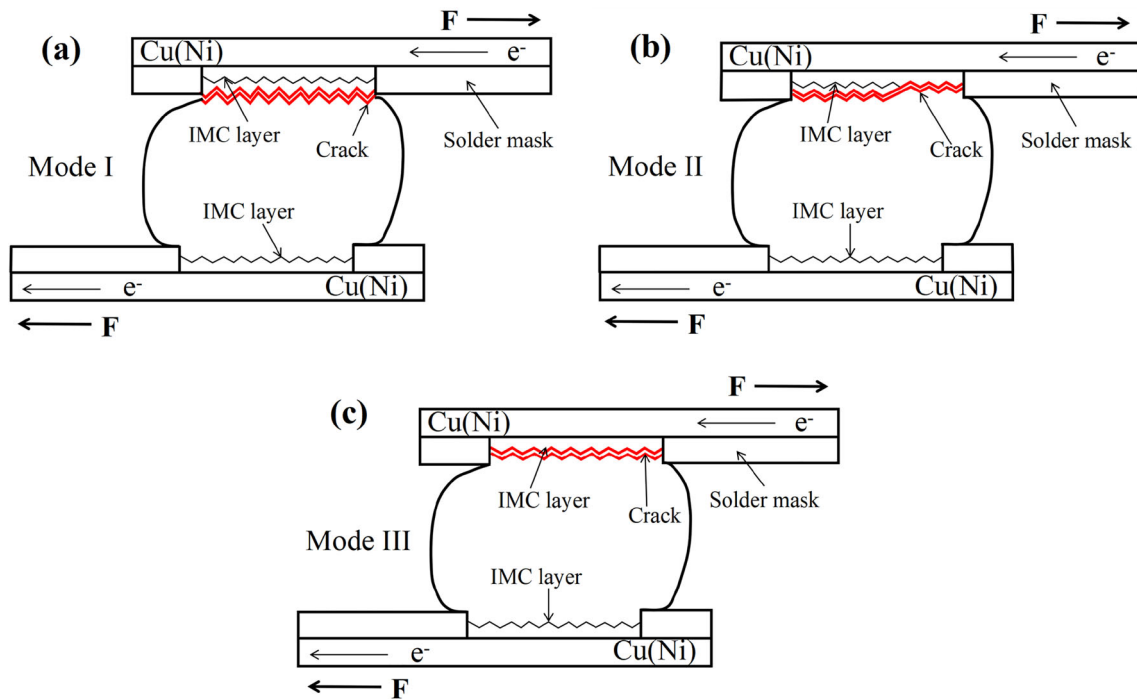
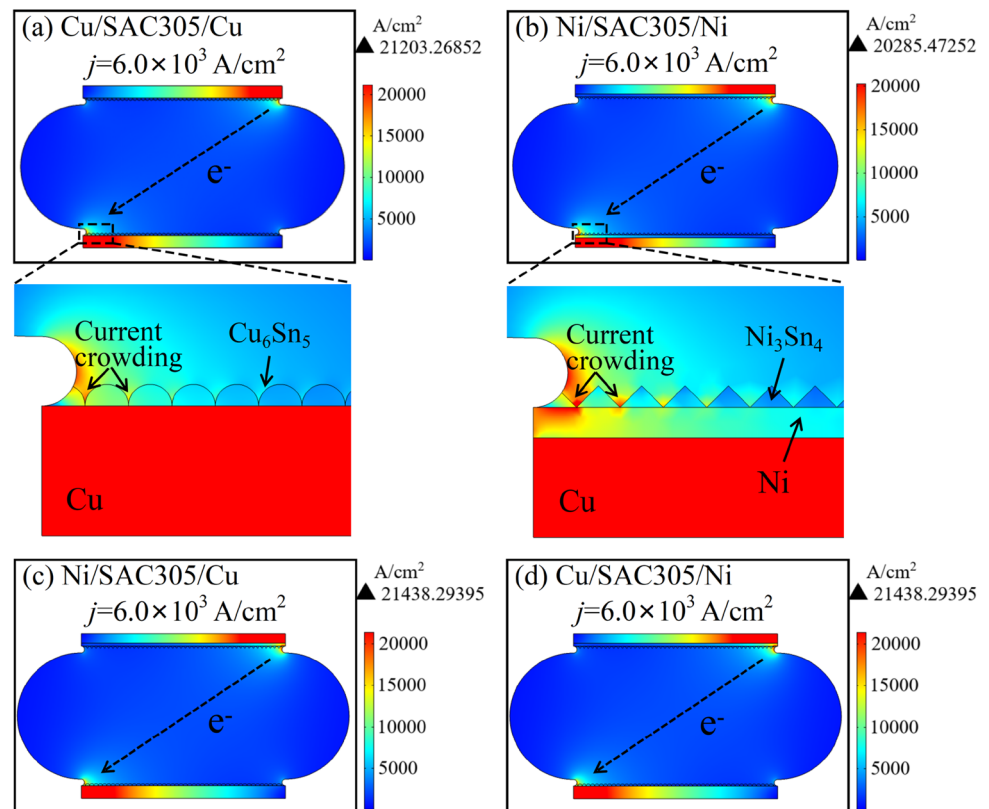


**Fig. 14** Schematic of the fracture modes in the BGA-structured Cu(Ni)/SAC305/Cu(Ni) solder joints under ETM coupled loads, **a** mode I: ductile fracture in the solder matrix, **b** mode II: mixed

ductile and brittle fracture in the solder matrix and at the solder/IMC layer interface, and **c** mode III: brittle fracture at the solder/IMC layer interface

**Fig. 15** Current density distribution of the BGA-structured solder joints under a current density of  $6.0 \times 10^3$  A/cm<sup>2</sup>, **a** Cu/SAC305/Cu, **b** Ni/SAC305/Ni, **c** Ni/SAC305/Cu, and **d** Cu/SAC305/Ni



Similar to the deformation, the fracture behavior can also be analyzed in terms of Joule heating. Owing to the inhomogeneities in the configuration and microstructure of the BGA-structured Cu(Ni)/SAC305/Cu(Ni) solder joints, the current density distributes inhomogeneously in the solder joints, which can result in an uneven Joule heating-induced rise in temperature. To better understand the local thermal state in the solder joints under ETM coupled loads, the current density distribution in the solder joints was simulated and presented in Fig. 15. Current crowding occurred at the grooves of the interfacial IMC grains and was most prominent at the groove of interfacial IMC grains closest to the electron flow entrance and exit corners, as shown in Fig. 15a and b. A similar current density distribution is obtained for the Ni/SAC305/Cu and Cu/SAC305/Ni solder joints, as shown in Fig. 15c and d. Accordingly, hot spots are more likely to form at the current crowding site first. Once the temperature of the hot spots exceeds the melting point of the SAC305 solder, local melting occurs at the solder side, where microcracks can be triggered.

The solder/IMC layer interface endures the most serious strain mismatch owing to the difference in CTE between the  $\text{Cu}_6\text{Sn}_5$  or  $(\text{Cu}, \text{Ni})_3\text{Sn}_4$  and SAC305 solder [42], as shown in Fig. 16. The propagation of the microcrack can be driven by the mismatch strain. As the electrical resistivity of the melted solder is higher than that of the solid-state one, current crowding remains at the frontier of the liquid/solid interface [23]. Thus, cracks are propagated along the solder/IMC layer interface, see Fig. 17. Moreover, the maximum equivalent strain at the solder/IMC layer interface increased with increasing current density, see Fig. 18. Accordingly, interfacial fractures are more likely to occur at high current densities.

## 5 Conclusion

In this study, the shear performance and fracture behavior of microscale BGA-structured SAC305 solder joints with different substrate surface finish combinations under ETM coupled loads were investigated by experimental characterization, theoretical

**Fig. 16** Equivalent strain distribution at a current density of  $6.0 \times 10^3 \text{ A/cm}^2$ , **a** Cu/SAC305/Cu, **b** Ni/SAC305/Cu, **c** Ni/SAC305/Ni, and **d** Cu/SAC305/Ni

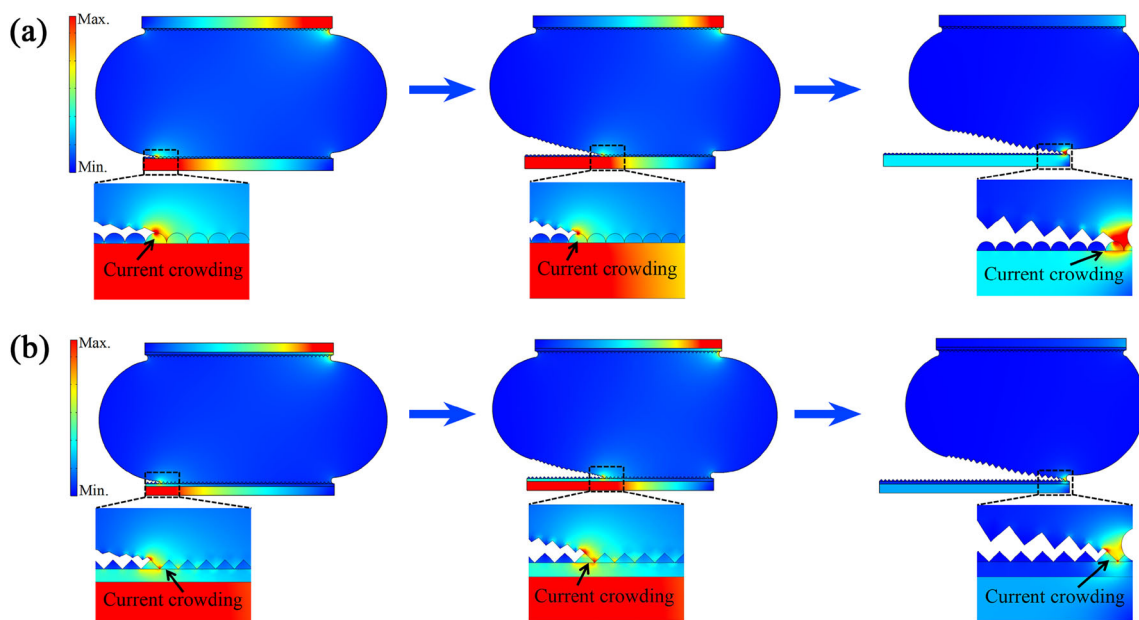
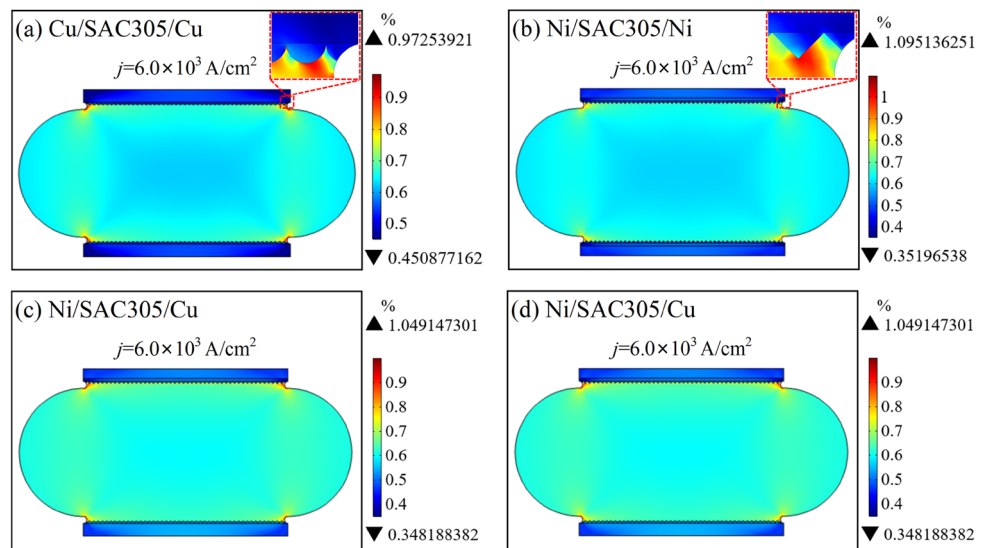


**Fig. 17** Current density distribution of the solder joints during crack propagation, **a** Cu/SAC305/Cu and **b** Ni/SAC305/Ni solder joints

analysis, and finite element simulation. The main conclusions are summarized as follows:

- (1) The shear strengths of the SAC305 solder joints with different substrate surface finish combinations were similar under ETM coupled loads. The shear strength first increased and then decreased with increasing current density.
- (2) The fracture location of the solder joints gradually changed from the solder matrix to the solder/IMC layer interface with increasing current density. In addition, an obvious ductile-to-brittle transition was noted.
- (3) The interfacial fracture was triggered by current crowding at the groove of the IMC grains close to the corners of the solder joints and was driven by the mismatch strain at the solder/IMC layer interface.

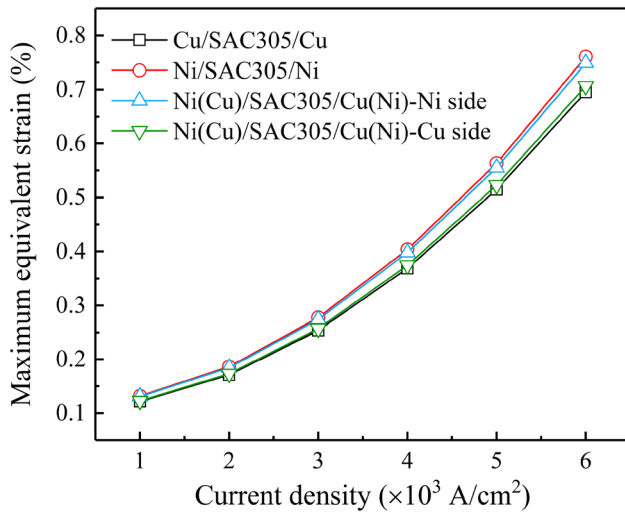


**Fig. 18** Maximum equivalent strain of the BGA-structured Cu(Ni)/SAC305/Cu(Ni) solder joints with different current densities

## Author contributions

BW contributed to methodology, data curation, formal analysis, and writing and preparation of the original draft. WL contributed to conceptualization, methodology, formal analysis, writing, reviewing, and editing of the manuscript, and funding acquisition. KP contributed to funding acquisition, conceptualization, and writing, reviewing, and editing of the manuscript.

## Funding

This research was funded by the National Natural Science Foundation of China under Grant No. 51805103, Natural Science Foundation of Guangxi Province under Grant No. 2018GXNSFBA281065, Science and Technology Planning Project of Guangxi Province under Grant No. GuiKeAD18281021, Director Fund Project of Guangxi Key Laboratory of Manufacturing System and Advanced Manufacturing Technology No. 19-050-44-003Z, Self-Topic Fund of Engineering Research Center of Electronic Information Materials and Devices Nos. EIMD-AA202007 and EIMD-AB202005, and Innovation Project of Guangxi Graduate Education Nos. YCBZ2021068 and JGY2021084.

## Data availability

The data that support the findings of this study are available from the corresponding author upon reasonable request.

## Code availability

The codes are not publicly available as they also form part of an ongoing study.

## Declarations

**Conflict of interest** The authors declare that they have no known competing financial interests or personal relationships that could have appeared to influence the work reported in this paper.

**Ethical approval** This article does not contain any studies with human tissues or animals performed by any of the authors.

**Consent to participate** This research is not related to human subjects.

**Consent for publication** The author assigns non-exclusive publication rights to Springer and warrants that his contribution is unique and that he possesses all necessary authority to make this grant. The author assumes responsibility for the material's release on behalf of all co-authors. This assignment of publication rights includes the non-exclusive right to reproduce and distribute the article in any format, including reprints, translations, photographic reproductions, microform, electronic form (offline, online), or other reproductions of a similar nature.

## References

1. J.W. Nah, J.O. Suh, K.N. Tu, *J. Appl. Phys.* **98**, 013715 (2005)
2. K.N. Tu, Y.X. Liu, M.L. Li, *Appl. Phys. Rev.* **4**, 011101 (2017)
3. W.Y. Li, H. Jin, W. Yue, M.Y. Tan, X.P. Zhang, *J. Mater. Sci.: Mater. Electron.* **27**, 13022 (2016)
4. W.K. Le, J.Y. Zhou, C.B. Ke, M.B. Zhou, X.P. Zhang, *J. Mater. Sci.: Mater. Electron.* **31**, 15575 (2020)
5. C. Kinney, T.K. Lee, K.C. Liu, J.W. Morris, *J. Electron. Mater.* **38**, 2585 (2009)

6. C. Kinney, J.W. Morris Jr., T.K. Lee, K.C. Liu, J. Xue, D. Towne, *J. Electron. Mater.* **38**, 221 (2009)
7. D.D. Maio, C. Murdoch, O. Thomas, C. Hunt, The degradation of solder joints under high current density and low-cycle fatigue. 11th International Thermal, Mechanical and Multi-Physics Simulation, and Experiments in Microelectronics and Microsystems (EuroSimE), **1** (2010)
8. Y. Zuo, L.M. Ma, S.H. Liu, Y.T. Shu, F. Guo, *J. Electron. Mater.* **44**, 597 (2015)
9. Y.F. Jiao, K. Jermstittiparsert, A.Y. Krasnopevtsev, Q.A. Yousif, *Mater. Res. Express* **6**, 106302 (2019)
10. W.Y. Li, H.B. Qin, M.B. Zhou, X.P. Zhang, The influence of imposed electric current on the tensile fracture behavior of micro-scale Cu/Sn–3.0Ag–0.5Cu/Cu solder joints. 15th International Conference on Electronic Packaging Technology (ICEPT), **1030** (2014)
11. W.Y. Li, H.B. Qin, M.B. Zhou, X.P. Zhang, *Chin. J. Mech. Eng.* **52**, 46 (2016)
12. X. M. Li, J. Gui, W.Y. Li, H. D. Yan, H.B. Qin, J.Q. Huang, D.G. Yang, Tensile performance of line-type microscale Cu/Sn–58Bi/Cu joints under electro-thermo-mechanical coupled loads. 21th International Conference on Electronic Packaging Technology (ICEPT), **1** (2020)
13. W.K. Le, X. Ning, C.B. Ke, M.B. Zhou, X.P. Zhang, *J. Mater. Sci.: Mater. Electron.* **30**, 15184 (2019)
14. W.K. Le, X. Ning, J.Q. Huang, M.B. Zhou, X.P. Zhang, 19th IEEE International Conference on Electronic Packaging Technology (ICEPT), **610** (2018)
15. W.K. Le, T. Sun, J.Y. Zhou, M.B. Zhou, X.P. Zhang, Effect of loading rate on the shear performance and fracture behavior of micro-scale BGA structure Cu/Sn–3.0Ag–0.5Cu/Cu joints under coupled electromechanical loads. 20th International Conference on Electronic Packaging Technology (ICEPT), **1** (2019)
16. H.Z. Wang, X.W. Hu, X.X. Jiang, *Mater. Charact.* **163**, 110287 (2020)
17. H.Z. Wang, X.W. Hu, X.X. Jiang, Y.L. Li, *J. Manuf. Process.* **62**, 291 (2021)
18. J. Shen, Z.M. Cao, D.J. Zhai, M.L. Zhao, P.P. He, *Microelectron. Reliab.* **54**, 252 (2014)
19. S. Fuller, M. Sheikh, G. Baty, C.U. Kim, T.K. Lee, *J. Mater. Sci.: Mater. Electron.* **32**, 2853 (2021)
20. Y. Liu, F.L. Sun, H. Zhang, T. Xin, C.A. Yuan, G.Q. Zhang, *Microelectron. Reliab.* **55**, 1234 (2015)
21. T. You, Y. Kim, W. Jung, J. Moon, H. Choe, *J. Alloys Compd.* **486**, 242 (2009)
22. J.M. Kim, M.H. Jeong, S. Yoo, C.W. Lee, Y.B. Park, *Microelectron. Eng.* **89**, 55 (2012)
23. W.Y. Li, X.P. Zhang, H.B. Qin, Y.-W. Mai, *Microelectron. Reliab.* **82**, 224 (2018)
24. T. Siewert, S. Liu, D.R. Smith, J.C. Madeni, Database for solder properties with emphasis on new lead-free solders. NIST Spec. Publ. (2002)
25. T. An, F. Qin, J.G. Li, *Microelectron. Reliab.* **51**, 1011 (2011)
26. H.B. Qin, X.P. Zhang, M.B. Zhou, J.B. Zeng, Y.-W. Mai, *Mater. Sci. Eng.: A* **617**, 14 (2014)
27. K.S. Kim, S.H. Huh, K. Suganuma, *Microelectron. Reliab.* **43**, 259 (2003)
28. R.Y. Tian, C.J. Hang, Y.H. Tian, J.Y. Feng, *J. Alloys Compd.* **777**, 463 (2019)
29. V.M.F. Marques, C. Johnston, P.S. Grant, *Acta Mater.* **61**, 2460 (2013)
30. C.L. Liang, K.L. Lin, *Mater. Charact.* **145**, 545 (2018)
31. Y.H. Liao, C.L. Liang, K.L. Lin, A.T. Wu, *AIP Adv.* **5**, 127210 (2015)
32. P.C. Liang, K.L. Lin, *J. Alloys Compd.* **722**, 690 (2017)
33. H.C. Huang, K.L. Lin, A.T. Wu, *J. Appl. Phys.* **119**, 115102 (2016)
34. J.R. Lloyd, *J. Phys. D: Appl. Phys.* **32**, R109 (1999)
35. S.W. Chen, C.M. Chen, W.C. Liu, *J. Electron. Mater.* **27**, 1193 (1998)
36. L.H. Xu, J.H.L. Pang, K.N. Tu, *Appl. Phys. Lett.* **89**, 221909 (2006)
37. B. Chao, S.H. Chae, X.F. Zhang, K.H. Lu, J. Im, P.S. Ho, *Acta Mater.* **55**, 2805 (2007)
38. G.I. Taylor, *Proc. R. Soc. London* **145**, 362 (1934)
39. W.J. Poole, M.F. Ashby, N.A. Fleck, *Scr. Mater.* **34**, 559 (1996)
40. P. Zhang, S.X. Li, Z.F. Zhang, *Mater. Sci. Eng.: A* **529**, 62 (2011)
41. H.J. McQueen, W. Blum, *Mater. Sci. Eng.: A* **290**, 95 (2000)
42. J.W. Elmer, E.D. Specht, *J. Electron. Mater.* **40**, 201 (2011)

**Publisher's Note** Springer Nature remains neutral with regard to jurisdictional claims in published maps and institutional affiliations.